CONTENTS

4. Carbon Nanotubes 87

4.1. Introduction 87

4.2. Structure and properties of carbon nanotubes (CNTs) 88

4.2.1. The structure of carbon nanotubes 88

4.2.2. Electronic structure 89

4.2.3. Optical properties 90

4.2.4. Nonlinear optical properties. 92

4.2.5. High harmonics generation mechanism in carbon nanotubes 93

4.3. Experimental studies 96

4.3.1. The samples 96

4.3.2. Optical characterisation of CNTs 98

4.3.3. Experimental setup for harmonics investigation 100

4.3.4. Harmonics generation 102

4.3.5. Continuum generation 107

4.4. Conclusions 112

CHAPTER 4

CARBON NANOTUBES

4.1 Introduction

Carbon nanotubes have diameters in the nanometer range and lengths of micrometers. This particular structure leads to remarkable electronic and optical properties, combining one-dimensional solid-state characteristics with molecular dimensions. While their structure has extensively been studied by means of electron and tunnelling microscopy, only few experimental studies have been reported on their optical properties. In particular, the nonlinear optical properties have been studied mainly theoretically. Only two experimental investigations on third order nonlinearities using nanotube suspensions have been reported [LSC99, WHY00]. A very interesting theoretical study from Slepyan et al. [SMK99, SMK01] predicted a new high harmonics generation mechanism from arrays of aligned carbon nanotubes. The scope of the present work is to investigate the nonlinear optical effects induced by high intensity ultrafast laser pulses in such samples of aligned carbon nanotubes.

A summary of the structure and properties of carbon nanotubes is presented in the second section of this chapter. Section 4.2.1 gives an introduction on the structure of carbon nanotubes. The peculiar dependence of the electronic properties on this structure is discussed in Section 4.2.2. Theoretical aspects of the optical absorption and nonlinear optical properties are reviewed in Sections 4.2.3 and 4.2.4, respectively. The mechanism for the generation of high harmonics in nanotubes is discussed in 4.2.5. The experimental studies are presented in the third section of the chapter. The samples used in the present measurements and their characterisation by optical absorption are shown in Sections 4.3.1 and 4.3.2. The experimental setup for the measurement of third and fifth harmonic generation is described in Section 4.3.3, while the experimental results are presented in Section 4.3.4. The interaction of high intensity lasers with samples of

carbon nanotubes mainly results in the generation of white light. Possible mechanisms for this continuum generation are discussed in Section 4.3.5 and the conclusions are given in Section 4.4.

4.2 Structure and properties of carbon nanotubes

4.2.1 The structure of carbon nanotubes

The structure of carbon nanotubes (CNTs) is, with respect to the bonding of carbon atoms and the orbitals hybridisation, essentially graphitic. The nanotubes are cylinders formally obtained by rolling a graphene sheet. Some of them have closed hemispherical caps where pentagons are inserted into the honeycomb lattice to get a large curvature, similar to the fullerenes. The circumference of any CNT can be expressed in terms of its chiral vector

$$\vec{C}_h = n \cdot \hat{a}_1 + m \cdot \hat{a}_2 \tag{4.1}$$

connecting two crystallographically equivalent sites on a 2D graphene sheet [DDS92]. $\hat{a}_1$ and $\hat{a}_2$ are the unit vectors of the hexagonal honeycomb lattice, as shown in Fig.4.1.

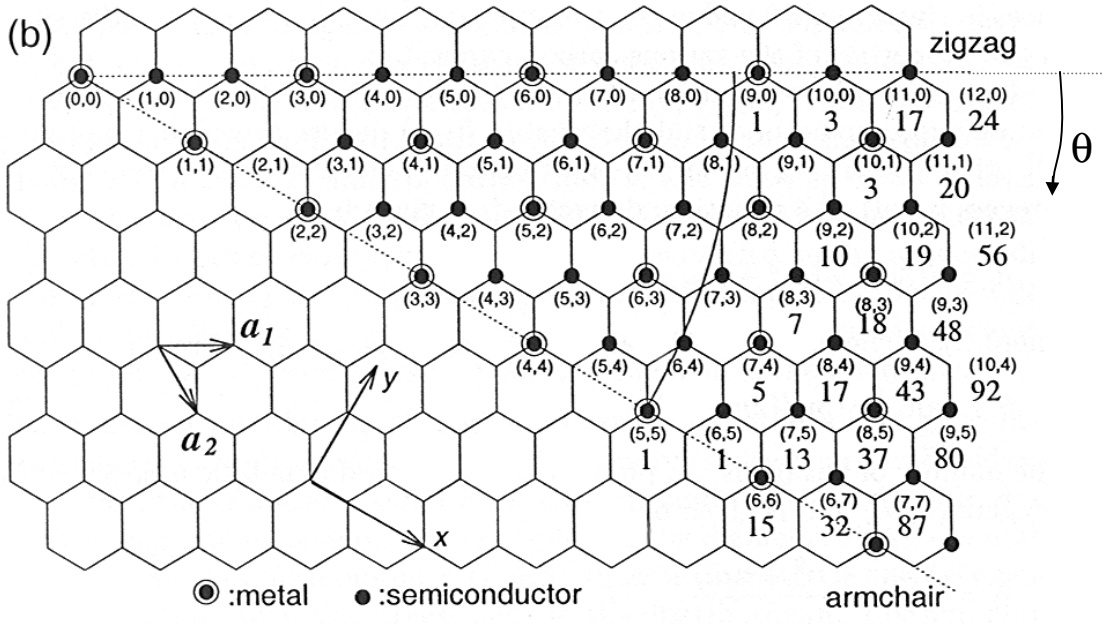

Fig.4.1. Possible $\vec{C}_h$ vectors specified by the (n,m) indices for general CNTs. $\hat{a}_1$ and $\hat{a}_2$ are the unit vectors of the hexagonal lattice. Small dots indicate semiconducting nanotubes, while encircled dots denote the metallic nanotubes. Below the (n,m) pair of integers, the number of distinct caps that can be joined continuously to the CNT is indicated [DDE96].

The nanotube diameter will then be $d_{CNT} = C_h/\pi$, the chiral angle $\theta = tan^{-1}[\sqrt{3}\, n/(2m+n)]$, and the number of hexagons per unit cell $N = 2(m^2+n^2+nm)/d_R$, where $d_R = d$ if $n - m \neq 3d$ and $d_R = 3d$ if $n - m = 3d$. Any CNT is thus fully defined by the pair of indices *(n,m)*. Fig.4.1 shows a series of possible vectors $\vec{C}_h$ specified by the indices *(n,m)* for general CNTs. The special classes with *(n,0)* indices where $\theta = 0°$ form the so-called called zigzag nanotubes, while *(n,n)* pairs with $\theta = 30°$ generate the armchair nanotubes.

Depending on the particular experimental conditions, either single walled CNTs (SWCNTs), with typical diameters of 1-2 nm, or multiwalled CNTs (MWCNTs) can be synthesised. A MWCNT is composed of several coaxial tubes (see Fig.4.2), each of which can be described by a chiral vector $\vec{C}_h$, with increasing diameters.

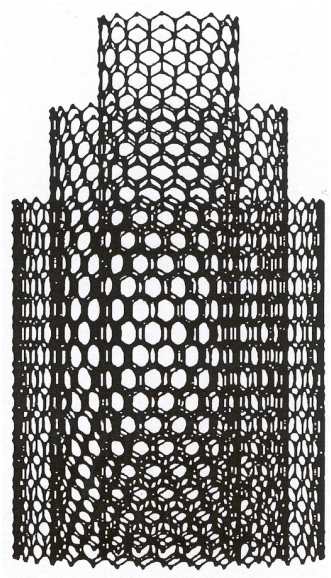

Fig.4.2. Schematics of a MWCNT consisting in three concentric tubules [Ber00].

The stacking of the cylinders is not correlated, and the interlayer spacing of ~ 0.34 nm [Iij91] is close to that of turbostratic graphite (0.344 nm). The interaction between the adjacent layers in MWCNTs is weak, and the properties of such tubes can be simulated by considering them as an ensemble of diameter distributed SWCNTs [MGZ01].

4.2.2 Electronic structure

For small diameters, the curvature and cylindrical symmetry give rise to sizeable quantum effects [DDS92, SFD92]. The nanotubes have a one-dimensional (1D) electronic band structure, derived by zone-folding of the two-dimensional (2D) band structure of graphene onto the

1D Brillouin zone of the tubes. The tight-binding π band structure of 2D graphite sheet is expressed by [SFD92]:

$$E_{g2D}(k_x,k_y) = \pm\gamma_0\left\{1+4\cos\left(\frac{3bk_x}{2}\right)\cos\left(\frac{\sqrt{3}bk_y}{2}\right)+4\cos^2\left(\frac{\sqrt{3}bk_y}{2}\right)\right\}^{1/2}, \quad (4.2)$$

where γ_0 is the nearest-neighbour C-C energy overlap integral and b is the interatomic distance in the graphite sheet. With the periodic boundary condition for an armchair (n,n) nanotube:

$$3bnk_x^q = q2\pi, \qquad q = 1,..., n, \quad (4.3)$$

the energy dispersion relation for the (n,n) armchair nanotube becomes [SFD92]:

$$E_q^a(k) = \pm\gamma_0\left\{1+4\cos\left(\frac{q\pi}{n}\right)\cos\left(\frac{\sqrt{3}bk}{2}\right)+4\cos^2\left(\frac{\sqrt{3}bk}{2}\right)\right\}^{1/2} \quad (4.4)$$

$$-\frac{\pi}{\sqrt{3}} < kb < \frac{\pi}{\sqrt{3}}, \qquad q = 1,..., n.$$

Similarly, for a zigzag nanotube (n,0) the boundary conditions are

$$\sqrt{3}bnk_y^q = q2\pi, \qquad q = 1,..., 2n \quad (4.5)$$

and the energy dispersion [SFD92]

$$E_q^z(k) = \pm\gamma_0\left\{1+4\cos\left(\frac{q\pi}{n}\right)\cos\left(\frac{3bk}{2}\right)+4\cos^2\left(\frac{q\pi}{2}\right)\right\}^{1/2} \quad (4.6)$$

$$-\frac{\pi}{3} < kb < \frac{\pi}{3}, \qquad q = 1,..., 2n.$$

Depending on their structure, the tubes are either metallic or semiconducting, although the local chemical bonding or coordination of the carbon atoms is the same. When $n-m=3q$ (with q an integer) the nanotube is metallic and when $n-m\neq 3q$, it is a semiconductor [SFD92, DDS92]. As the tube diameter increases, the curvature decreases and the semiconducting band gap disappears. Scanning tunnelling spectroscopy (STS) revealed that, for tubes larger than ~ 30 nm, the STS spectra are similar to the spectrum of graphite and the characteristic quantic features of CNTs with small diameters are not observable [BBT01].

4.2.3 Optical properties

The nanotube density of states (DOS) exhibits a series of characteristic van Hove singularities. The energy differences $E^M_{11}(d_{CNT})$ and $E^S_{11}(d_{CNT})$ for metallic and semiconducting nanotubes between the highest-lying valence band singularity and the lowest-lying conduction band singularity in the 1D electronic density of states curves are expressed as [SDD00]:

$$E^{M}_{11}(d_{CNT}) \cong 6b\gamma_0 / d_{CNT} \quad \text{and} \quad E^{S}_{11}(d_{CNT}) \cong 2b\gamma_0 / d_{CNT}\,, \tag{4.7}$$

with b the nearest-neighbour carbon-carbon distance (0.142 nm) and γ_0 the overlap integral (2.9 - 3 eV). Optical transitions $E_{pp'}$ from the p-th valence band to the p'-th conduction band occur in accordance with the selection rules $\delta p=0$ and $\delta p=\pm 1$ for parallel and perpendicular polarisations of the electric field with respect to the nanotube axis, respectively. In the case of perpendicular polarisation, the optical transition is suppressed by the depolarisation effect [AjA94], so that optical absorption only occurs for $\delta p=0$. Fig.4.3 shows the values of $E^{S}_{pp}(d_{CNT})$ and $E^{M}_{pp}(d_{CNT})$ as a function of nanotube diameter for all chiral angles [SDD00, KKM99, AjA94]. The width of the $E_{ii}(d_{CNT})$ curves depends on the chirality of the tubes, as discussed in [SDD00].

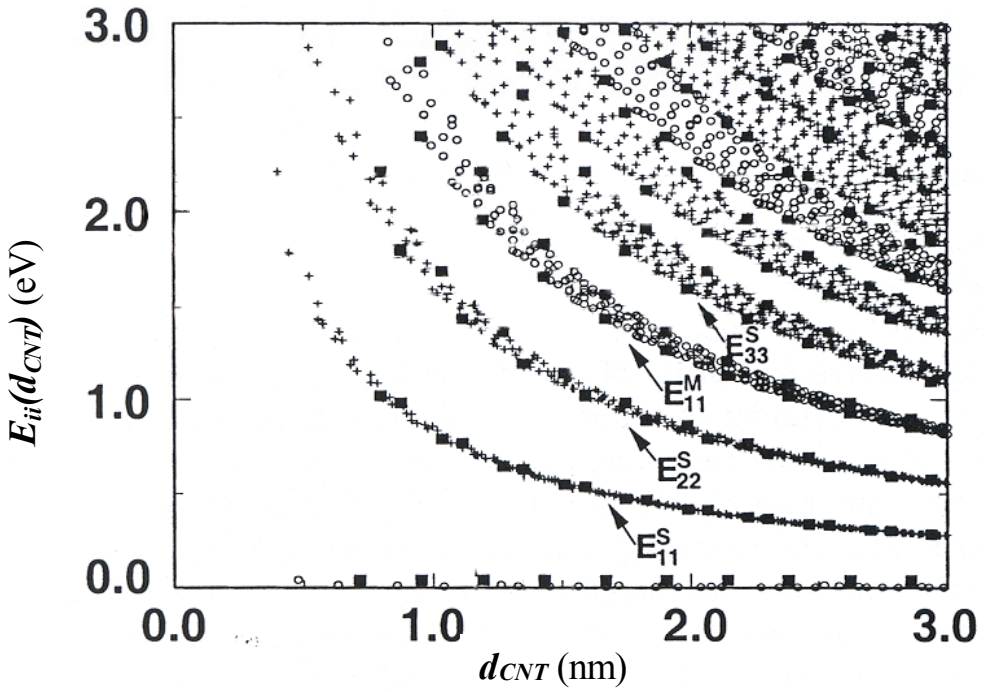

Fig.4.3. Energy separations $E_{ii}(d_{CNT})$ for all (n,m) values versus nanotube diameter in the range $0.7<d_{CNT}<3.0$ nm, Semiconducting and metallic nanotubes are indicated by crosses and open circles, respectively. The filled squares denote zigzag tubes [Dre01].

This plot is very useful for the interpretation of optical absorption spectra from SWCNTs. For a sample of tubes with selected diameters, normally containing both metallic and semiconducting tubes, optical transitions will appear at the energies $E^{S}_{11}(d_{CNT})$, $2E^{S}_{11}(d_{CNT})$, $E^{M}_{11}(d_{CNT})$, $4E^{S}_{11}(d_{CNT})$, ...; their intensity is decreasing with increasing the energy. Very good agreement was found between these theoretical predictions and measured optical absorption spectra from samples of SWCNTs with a narrow diameter distribution [KKM99, JGP99,

KMY00]. For a broad diameter distribution, the superposition of the spectral lines corresponding to SWCNTs of different sizes results in strong broadening, intensity decrease and shifting of the peaks [MaG01]. These resonant transitions overlap on broad π-electronic collective excitations (π plasmons), having a prominent peak at 5 - 7 eV. This peak is common for all CNTs and its position does not depend on the diameter and chirality of the nanotubes [LiS94].

In the case of MWCNTs, the weak intertube interactions only affect the low-energy electronic structure for $E < 0.1$ eV [KwT98]. The independent tube approximation is thus reasonably employed for estimating the properties of the tubes for $\omega > 0.1$ eV. The calculated [LSC00] and measured [HBC95, BDW96, BDW97] optical reflectivity from samples of aligned MWCNTs shows that the specific peaks, characteristic for the resonant transitions in SWCNTs, disappear from the spectrum due to the superposition of the contributions from the coaxial nanotubes. The only prominent feature in the spectrum remains the broad π-plasmon peak at $\omega \sim \gamma_0$, around 6 eV.

4.2.4 Nonlinear optical properties.

Theoretical calculations [XiJ98, JDX99, MGZ01] have shown that the large number of π-conjugated electrons in CNTs leads to enhanced third-order nonlinear-optical effects. Only two experiments have been reported so far, using backward degenerate four-wave mixing in solutions of MWCNTs [LSC99] and femtosecond optical Kerr technique with solutions of SWCNTs [WHY00]. Both experiments have shown that the contribution from each carbon atom to the second-order hyperpolarisability ($\gamma_c = 7.7 \cdot 10^{-33}$ esu in SWCNTs and $5.9 \cdot 10^{-36}$ esu in MWCNTs) is larger than in the C_{60} fullerene ($\gamma_c = 1.5 - 5 \cdot 10^{-36}$ esu). The γ_c value found for SWCNTs is much larger than the one for MWCNTs, which is in good agreement with the theoretical prediction of an overall suppression of the TH intensity from samples with a large diameter distribution of the tubes [MGZ01]. No experiments on solid samples of CNTs have been reported so far.

Higher-order optical nonlinearities, more exactly high harmonics generation (HHG) from a single armchair or zigzag SWCNT excited by a linearly polarised intense radiation have first been theoretically predicted by Slepyan et al. [SMK99]. Phase matching conditions in ropes of aligned SWCNTs has been considered in [SMK01]. This model is discussed in more detail in Chapter 4.2 and an experimental test of this theory is discussed in Chapter 4.4. Alon et al.

[AAM00] have also estimated the HHG spectra from chiral isolated SWCNTs interacting with a circularly polarised laser field, based on symmetry selection rules (the generation mechanism was not taken into consideration). The high HHG efficiency suggested by the calculations would recommend the nanotubes as nanometre scale soft X-ray sources.

4.2.5 High harmonics generation mechanism in carbon nanotubes

Generation of high harmonics is typically observed from the interaction of subpicosecond laser pulses at an intensity of ~ 10^{15} W/cm^2 with gaseous targets [e.g. MKG93, LHB93]. The theoretical models for this process [e.g. Cor93] explain the harmonics generation in the strong-field regime by electron tunnelling to the continuum and recombination with the atomic core under the action of the oscillating field. High harmonics generation is also observed for the interaction of intense laser pulses (~10^{17} W/cm^2) with solid targets [LEJ95, NZM96]. In this case, a plasma with a maximum free-electron density of the solid is formed, showing an almost step-like density profile at the plasma-vacuum interface. The normal component of the laser field will drive the electrons to oscillate anharmonically at close to relativistic velocities across this sharp plasma-vacuum interface [Gib96], giving rise to radiation at odd- and even-harmonics of the driving fundamental laser frequency.

Recently, a third fundamental mechanism for HHG was proposed by Slepyan et al [SMK99, SMK01]. The high-order harmonics could be generated by conduction electrons confined at the cylindrical surface of a metallic carbon nanotube illuminated by an intense laser pulse. Conduction electrons with energies below the energy of the interband transitions move in the crystalline field like free quasiparticles with a modified nonparabolic dispersion law that enhances strongly their nonlinearity. An array of identical and spatially homogeneous SWCNTs, of thickness L, is considered in [SMK01], with the surface of the sample in the (x,z) plane – as shown in Fig.4.4. A linearly p-polarised laser beam is incident on this sample at an angle θ.
The high harmonics are generated by oscillations of the electron surface current, excited by this incident laser pulse. The azimuthal current on the CNT surface is neglected, assuming the contribution of the axial current to be predominant, therefore this process is sensitive to the polarisation of the driving field. In an aligned array of CNTs, only the field component parallel to the CNT axis contributes to the HHG process. High-order harmonics radiation is produced by longitudinal oscillations of electrons that do not cross the boundaries of CNTs.

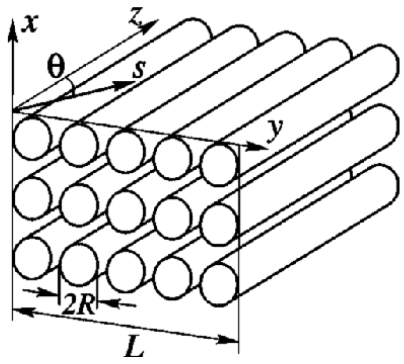

Fig.4.4. Scheme of an aligned sample of SWCNTs [SMK01].

The following approximations were used in this semiclassical approach: the interband, resonant transitions as well as interband tunnelling and formation of free electrons are neglected, thus limiting the driving-field frequency and strength, respectively. The relaxations of the electrons are also neglected, which holds for laser pulses shorter than the mean time of the electron free path, taken to be 3 ps [JDD93, HBA00].

The limitation on the driving field frequency ω imposed by the condition that resonant transitions are negligible will give, taken into consideration the low-frequency edge $\overline{\omega} = \frac{E_{11}(d_{CNT})}{\hbar}$ of the transition band in CNTs (see equation (4.7)):

$$\omega < \overline{\omega} = \begin{cases} \dfrac{6\gamma_0 b}{\hbar \cdot d_{CNT}} & \text{for metallic CNTs} \\ \dfrac{2\gamma_0 b}{\hbar \cdot d_{CNT}} & \text{for semiconducting CNTs} \end{cases} \tag{4.8}$$

γ_0 is the overlap integral (~ 3 eV for carbon) and b = 0.142 nm the interatomic distance in graphene.

To avoid the formation of free electrons, the Stark frequency induced by the strength of the driving field must be smaller than the conduction-zone bandwidth, giving the limiting condition for the field strength:

$$A < 2\gamma_0 / e d_{CNT} . \tag{4.9}$$

The numerical results of this calculation showed high conversion efficiency for the HHG from metallic tubes, while the conversion in semiconducting tubes was found to be orders of magnitude lower. The high-order harmonic yield is independent of the diameter of the metallic tubes, which is not the case for the semiconducting ones. The specific character of the electron

dispersion law in CNTs gives a peculiar HHG spectrum with a smooth decrease in the harmonic intensity with the increase of the harmonic order, instead of the cut-off found from gases or solid targets.

Only the results of the calculations for the third and fifth harmonics, which were studied in our experiments, are shown here. Fig.4.5 shows the laser power dependence of these harmonics, calculated in the semiclassical approach for bundles of zigzag single walled tubes, either metallic (9,0) or semiconducting (10,0).

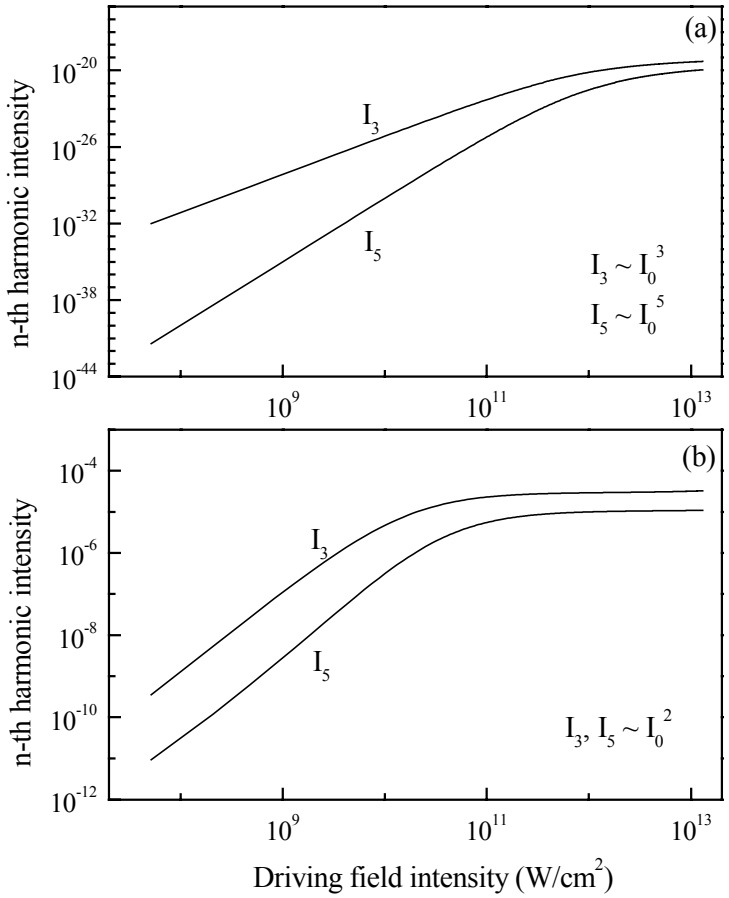

Fig.4.5. Calculated power dependence (in the semiclassical approach) of the third and fifth harmonics from aligned ropes of (a) metallic (9,0) and (b) semiconducting (10,0) SWCNTs [HeK00].

The harmonic yield from the metallic tubes shows a very unusual power dependence: both third and fifth harmonic intensities increase with the power of two in the input intensity. The same behaviour was found for armchair (*n,n*) tubes (which are all metallic) of different diameters. Although the separation of the metallic tubes from the semiconducting ones is so far experimentally not feasible, this unusual behaviour can be tested experimentally using samples of aligned tubes, since the metallic tubes should have a dominating harmonic yield, tens of orders of magnitude higher than the semiconducting tubes. However, care must be taken with

the data interpretation based on this simulation. The semiclassical approximation does not describe the semiconducting tubes correctly, while for the metallic ones it shows a good agreement with an improved full quantum-theoretical approach, recently developed by Slepyan et al. [SMK02].

In our experiments, we used samples of aligned MWCNTs with an outer diameter of ~ 20 nm, excited by a laser with a wavelength of 1250 nm, corresponding to a photon energy of 0.99 eV. The maximum metallic nanotube diameter for which condition (4.8) is fulfilled $d_{CNT} = 6\gamma_0 b / \hbar\overline{\omega}$ will be ~ 2.6 nm, while the semiconducting tubes may have a diameter of up to 0.86 nm. MWCNTs are formed by concentric nanotubes with different diameters. These nanotubes weakly interact with each other and the MWCNTs can be generally regarded as a heterogeneous sample of SWCNTs with a large diameter distribution [MGZ01]. We can expect that the theoretical requirement $\omega < \overline{\omega}$ be met for the inner metallic tubes from the MWCNTs in our samples. Considering now condition (4.9) for tubes with 2.6 nm diameter, we find that the input driving strength should be lower than $2.3 \cdot 10^9$ V/m. This corresponds to an intensity of the incident radiation $I = \varepsilon_0 \cdot c \cdot A^2 = 1.4\ 10^{12}$ W/cm^2.

4.3 Experimental studies

4.3.1 The samples

Different production methods for aligned MWCNTs have been reported in the literature so far [HBC95, LXQ96, TSW98, RFC00]. The samples used in our experiments, consisting of self-standing multiwalled CNTs aligned perpendicular on Si(001) substrates, were deposited by thermal CVD using a mixture of acetylene, hydrogen, iron pentacarbonyle and argon in 750 °C furnace, a method described in [RFC00]. Fig.4.6 shows two typical scanning electron microscopy (SEM) images of the samples, on two different scales. A high degree of alignment of the CNTs perpendicular to the substrate can be observed in this figure.

The tubes have a typical diameter of ~ 20 nm and lengths of more than 15 μm. The influence of the substrate on the optical measurements is negligible for such a thickness and we can treat the sample as a bulk of aligned MWCNTs. A sample with not-aligned CNTs was prepared to estimate the alignment effect on our measurements. A part of the aligned nanotubes film was removed from the Si substrate ultrasonicated in ethanol and a droplet of this suspension was

dried on a new silicon substrate. The film thus formed was composed by small domains (< 50 μm) of well aligned tubes, domains that are arbitrarily oriented on the substrate.

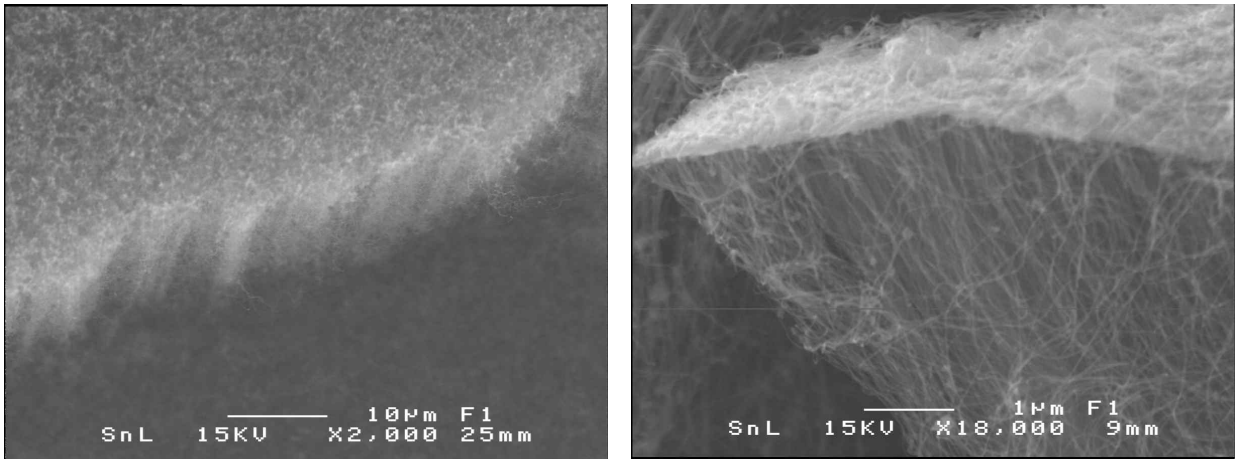

Fig.4.6. Scanning electron micrographs of a sample of aligned carbon nanotubes [Roh01].

A similar sample with not-aligned tubes was prepared using MWCNTs with selected diameters of around 5 nm. A "bucky paper" consisting of a mat of entangled purified SWCNT bundles was also used for comparison. The tubes were produced by a 90 A arc discharge in 660 mbar He using Ni/Y – filled graphite electrodes [Man01]. Though tubes of the same kind are typically aligned within a SWCNT bundle (see Fig.4.7), there is no alignment between the bundles.

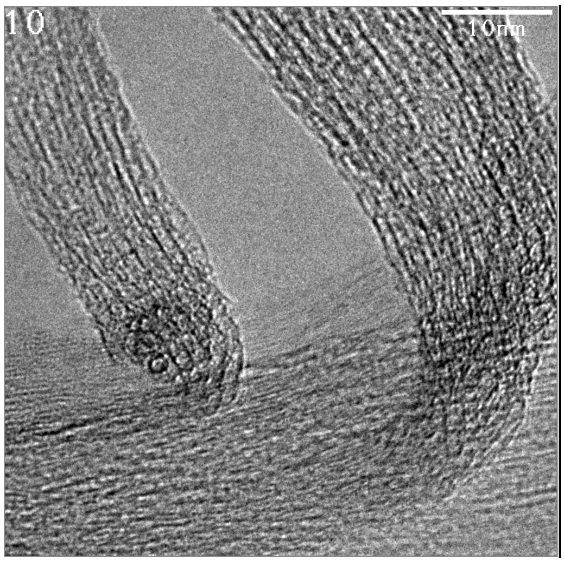

Fig.4.7. High-resolution transmission electron micrograph of bundles of SWCNTs [Man01].

The optical absorption of these tubes, giving information on their diameter distribution, is discussed in the following section.

4.3.2 Optical characterisation of the CNTs

Optical absorption spectra of samples of MWCNTs (with outer diameters of ~ 20 nm) and SWCNTs are shown in Fig.4.8. The samples were thin films prepared by drying low concentrated suspensions of the tubes on quartz plates. The spectra were measured with a Lambda 900 Perkin Elmer spectrometer. Both samples have a finite absorption over the whole energy region measured here, given by the π-electron plasma absorption background [HBC95, LSC00, KMY00]. The absorption in the region of low energy is stronger for the MWCNTs (relative to the absorption at higher energy), as expected from their larger diameters. No resonant features can be observed for this sample.

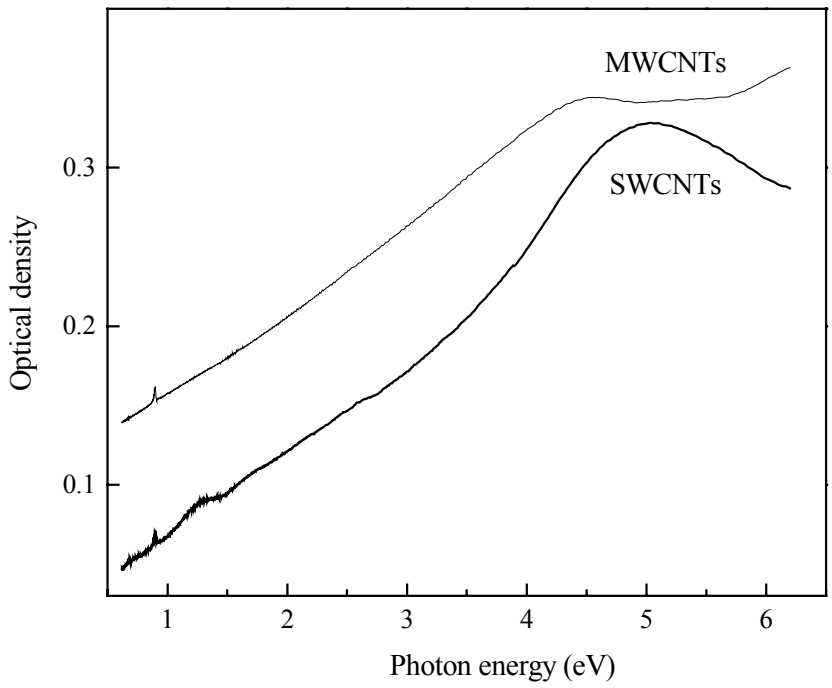

Fig.4.8. Optical absorption spectra of MWCNTs (thin line) and SWCNTs (thick line).

An interesting shift of the π-plasmon band from 5 eV for the SWCNTs, to ~ 4.5 eV for the MWCNTs can be observed in this spectrum. This does not agree with the theoretical predictions of Lin et al. [LiS94 and LSC00], saying that this plasmon should be insensitive to both radius and chiral angle of the tubes. The position of each of the peaks is, though, in good agreement with previously published absorption spectra of SWCNTs (see e.g. [KMY00]) and of MWCNTs

(from the maximum in the imaginary part of the dielectric function, ε_2, determined by ellipsometry in [HBC95]).

The resonant features are only weakly visible in the spectrum of the SWCNTs, probably due to residual amorphous carbon in the sample. After subtraction of the background (Fig.4.9), the absorption bands attributed to optical transitions between Van Hove singularities [KKM99] become more obvious. The sharp peak at 0.9 eV is due to absorption by the quartz substrate.

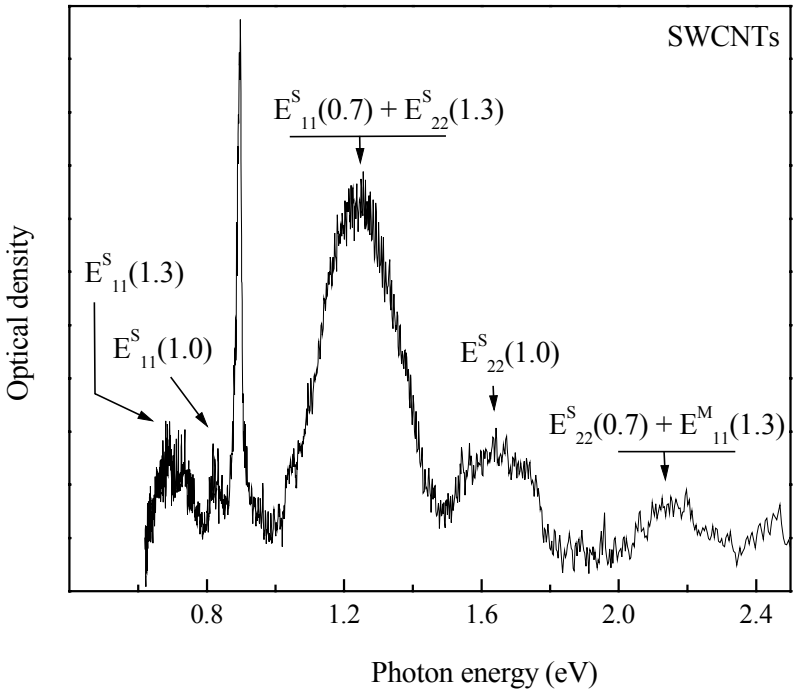

Fig.4.9. Optical absorption of the SWCNTs in the region 0.75- 2.00 eV after background subtraction, showing dipole-allowed transitions between van Hove singularities. The absorption bands $E^S_{ii}(d_{CNT})$ corresponding to tubes of different diameters are indicated in the figure; the diameter d_{CNT} is given in nanometres.

An unambiguous identification of these absorption bands by using the plot in Fig.4.3 is rather difficult, since the sample is quite heterogeneous. The strongest band is centred at ~ 1.23 eV. If we assign it to an $E^S_{11}(d_{CNT})$ transition, this would mean that the sample mainly contains tubes with a diameter of 0.7 ± 0.2 nm; the corresponding E^S_{22} transition is at ~ 2.1 eV, as indicated in the figure. If we assign the band at 1.23 eV to an E^S_{22} transition from the second valence band to the second conduction band, this would correspond to tubes with 1.3 ± 0.2 nm diameter. The corresponding $E^S_{11}(1.3)$ is then at ~ 0.67 eV and the metallic tubes of 1.3 nm will have their first absorption $E^M_{11}(1.3)$ at ~ 2.05 eV. A third large group of tubes, with diameters of around 1.0 nm, has the first absorption at ~ 0.82 eV and the second peak at ~ 1.65 eV. For these two last

groups of tubes, the first absorption is weaker than the second one, contrary to theoretical prediction and general experimental observations. Bleaching of E^S_{11}, though, has been observed by chemical modification of the tubes changing the population of the valence-band states, as reported in [KMJ99] and [PMJ99]. Hydroxylic, carboxylic or carbonylic groups can be added during the purification of the NT material in nitric acid. The chemical modification is also consistent with the formation of stable suspensions of the SWCNTs in water, which we found for our samples.

Raman spectroscopy measurements performed on these tubes indicate that they have diameters between 1.2 and 1.4 nm [Man01]. This would be in good agreement with the assignment of the strongest absorption peak at 1.23 eV to an E^S_{22} absorption from tubes with diameters centred around 1.3 nm.

4.3.3 Experimental setup for harmonics investigation

The optical setup used in the harmonic generation measurements is presented in Fig.4.10. We used a Cr:forsterite regenerative amplifier [SZP99] developed at Max Born Institute, which is operated with 1 kHz repetition rate, at 1.25 μm wavelength. The laser produces pulses of up to 200 μJ single-pulse energy, with a pulse duration of 160 fs (assuming a Gaussian pulse shape). This pulse width is much shorter than the mean time of the electron free path (3 ps) so that the electrons will not relax within the laser pulse, in good agreement with the theoretical requirement. The intensity of the beam can be tuned by rotating its polarisation by the means of a half-wave plate, in front of a polariser that was used to select either the s- or the p-polarisation with respect to the plane of incidence on the sample. When a full scan over the input polarisation was needed, the polariser was removed from the setup. The laser beam was focused on the sample with a 20 cm lens, to a spot of ~ 500 μm diameter. The beam was incident at an angle of 45° on the sample. At this angle of incidence, a p-polarised beam will have half of the electric field aligned parallel to the tubes. A 3 mm thick RG850 filter was placed right after the focusing lens, to remove all higher frequency light that is generated in the optical components from the beam path. The filter was slightly inclined from the normal orientation with respect to the incoming beam, in order to reflect a small fraction (~10%) onto a Newport 818J-09 energy detector, used to permanently monitor the energy of the beam during the measurements.

The samples of MWCNTs, either aligned or not aligned, are strongly scattering the laser beam, almost uniformly in a cone of ~ 2.1 rad. The scattering is caused by the high microscopic roughness of the samples, and is not of nonlinear origin: both the high-intensity femtosecond

laser beam and the weak He-Ne laser beam used for alignment are scattered in a similar way. A set of quartz lenses of 3 and 5 cm focal lengths and diameters of 5 and 4 cm, respectively, were used to focus the scattered light to a diameter of ~ 1 mm at the entrance slit of a Jobin Yvon H10-UV monochromator. The very broad scattering of the samples causes the deflection of the beam off the ideal geometrical path through the monochromator. This means that residual scattered photons with the energy of the input beam will strike the photomultiplier at the output of the monochromator, for any geometrical position of its dispersive element, together with the photons having an energy correctly selected by the grid. The scattered intensity is directly proportional to the intensity of the laser. The R955 photomultiplier is blind for the laser wavelength of 1250 nm, but sensitive when the laser is used at the second harmonic wavelength of 625 nm, so any photon scattered at this wavelength will contribute to the background.

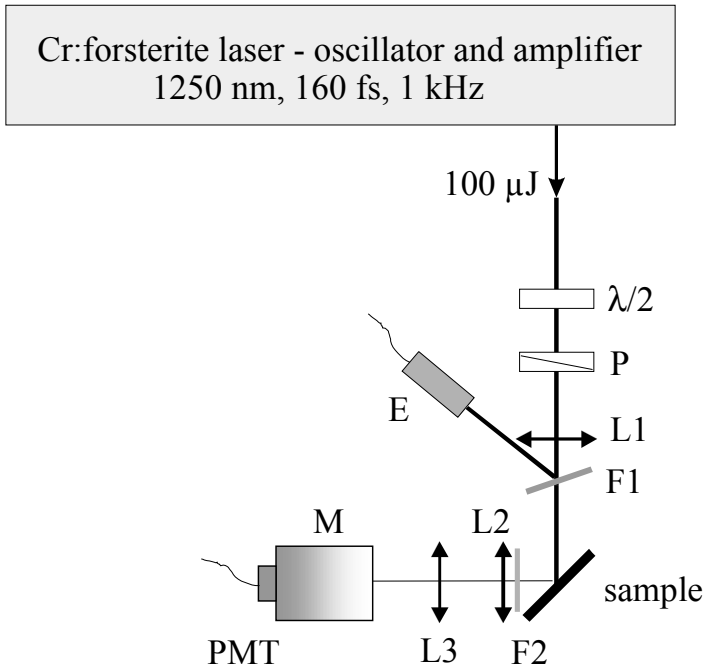

Fig.4.10. Experimental setup: λ/2, half-wave plate; P, polariser; L1, L2, L3, lenses of 20, 3 and 5 cm focal length, respectively; F1 is a RG850 filter, F2, KG5 filters; M, monochromator; PMT, photomultiplier; E, energy meter.

The spectral resolution of the monochromator was 4 nm. The signal was detected with a Hamamatsu R955 photomultiplier and recorded via a Stanford Instruments SR250 gated integrator. The gated integrator was dynamically averaging the signal over 300 pulses and each measured point was further averaged over 5000 laser shots.

4.3.4 Harmonics generation

The harmonics generation experiments were performed in air, with laser intensities of less than ~ $5 \cdot 10^{11}$ W/cm^2. For higher intensities, the film of CNTs was destroyed. Experiments performed under vacuum have shown damage of the sample at a laser intensity less than a factor of ten higher.

The interaction of high intensity lasers with all samples of CNTs mainly results in the generation of white light. A typical broad continuum spectrum generated by an s-polarised beam of $1.1 \cdot 10^{11}$ W/cm^2 from the not-aligned sample of MWCNTs with diameters of 5 nm is shown in Fig.4.11. The intensity profile is not corrected for the apparatus function given by the components of the setup described in the previous chapter. The only feature enhanced from the continuum background is at 417 nm, corresponding to the third harmonic of the laser.

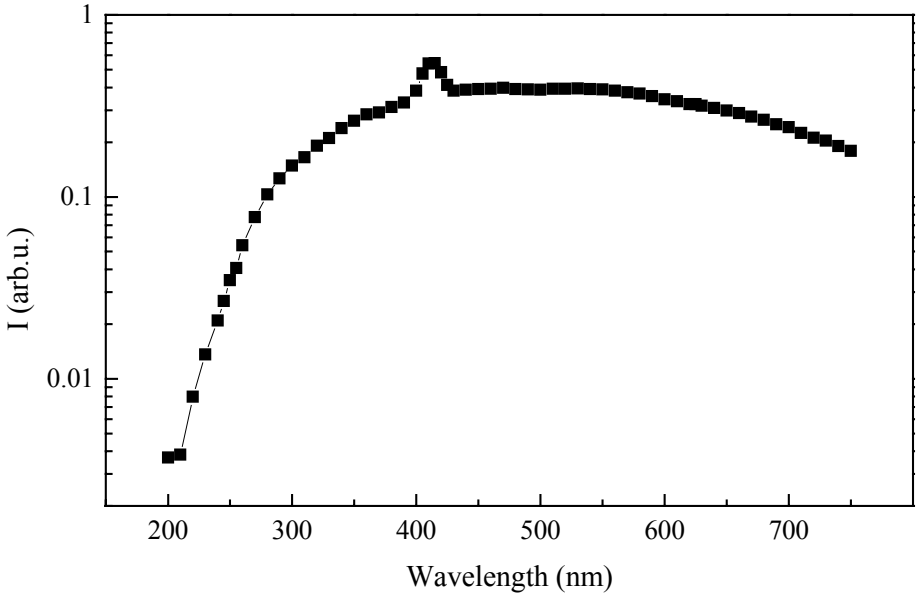

Fig.4.11. Continuous white light measured on the sample of not-aligned MWCNTs of 5 nm with an s-polarised beam of $1.08 \cdot 10^{11}$ W/cm^2 intensity. The spectrum is not corrected for the monochromator and the photomultiplier efficiencies.

The dependence of the unpolarised third harmonic (TH) on the input intensity was measured for the samples of aligned and not aligned tubes of 20 nm diameter and also for the not aligned sample of 5 nm tubes, both for s- and p-polarised input beams. Fig.4.12 shows the results obtained for a p-polarised input. The alignment of the tubes seems to slightly enhance the TH signal, while the tubes with smaller diameters clearly have a higher TH output. The signals start saturating at ~ $4 \cdot 10^{10}$ W/cm^2. The process responsible for this saturation behaviour is not clear.

Suspensions of CNTs in ethanol or water are known to behave as excellent broad band optical limiters [CWS99, VAR99, VRA00, MRM00]. The process responsible for this optical limiting in suspensions is nonlinear scattering, both by solvent vapour microbubbles formed by heat transfer from the absorbing CNTs to the solvent, and by the sublimation of the nanotube bundles. These processes can well explain the limiting behaviour of the suspensions, when irradiated with intense but long laser pulses, with pulse duration of nanoseconds, so that thermal effects are very important. Such effects can be excluded in our experiments. On the other hand, the reflected intensity from the solid films of CNTs starts to saturate at a significantly higher laser intensity of ~$2 \cdot 10^{11}$ W/cm^2, as shown in the inset of Fig.4.12.

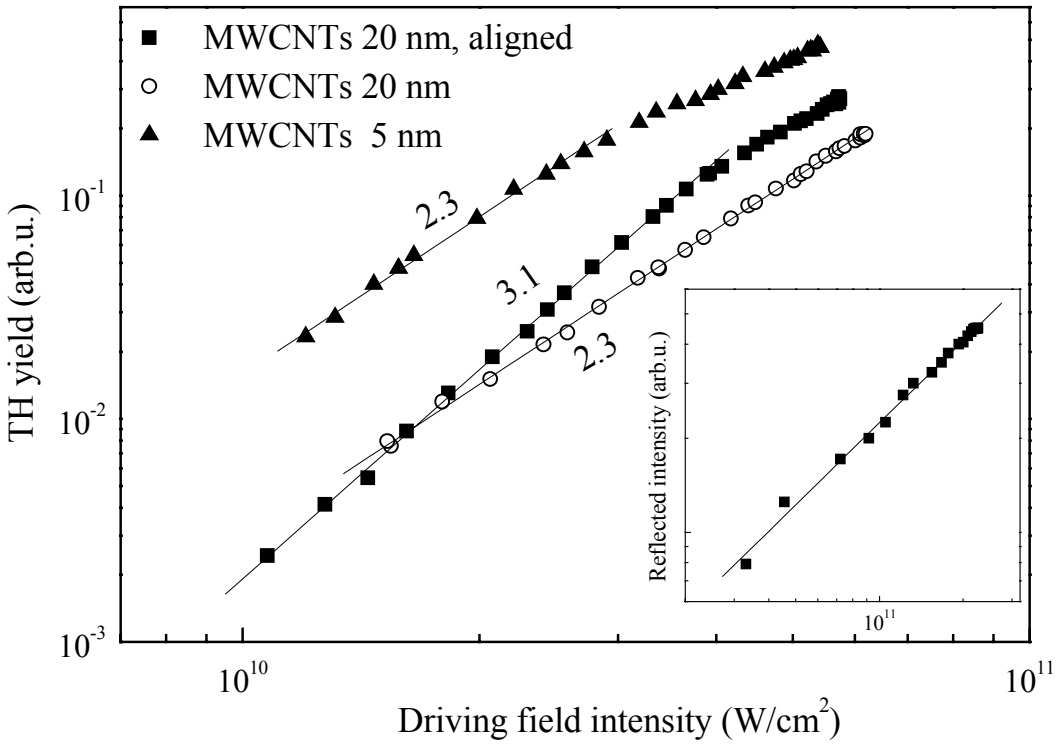

Fig.4.12. Power dependence of the THG, generated by a p-polarised input beam, from samples of aligned and not-aligned MWCNTs.
Inset: reflected intensity from the sample of aligned MWCNTs, with a power slope of ~1.

The slopes obtained by linear fits of the power dependence measurements are summarised in Table 4.1. The power dependence was also measured at 570 nm, which is a wavelength corresponding to the broad white continuum generated by all samples. Only the sample of aligned tubes shows a distinct power dependence of the THG on the input field, as $I_{TH} \sim I_{input}^3$. The power dependence for the samples of not-aligned tubes at 417 nm is similar to the slopes found for the white light at 570 nm, although the TH is enhanced from the broad continuum, as seen in the spectrum from Fig.4.11. One can assume that the generation of the light with

417 nm is in this case dominated by the process responsible for the generation of white light and not by a harmonic generation mechanism.

Wavelength detected →	417 nm (TH)		570 nm (white light)	
input polarisation →	s	p	s	p
MWCNTs 20 nm, aligned	3.0	3.1	2.5	2.4
MWCNTs 20 nm	2.5	2.3	2.1	2.2
MWCNTs 5 nm	2.7	2.3	2.6	2.6

Table 4.1. Slopes of the power dependence for the samples of MWCNTs, at the third harmonic wavelength of 417 nm and for the white light at 570 nm, for s- or p-polarised driving field; typical error for different spots on the sample ± 0.1.

Since the power dependence slope for the sample of not-aligned tubes does not show a saturation behaviour, like the sample of aligned tubes, we can also consider that at a certain intensity, the process responsible for the white light emission starts dominating over the harmonic generation mechanism at 417 nm, also for the aligned tubes.

The power dependence of 3 comes in contradiction with the theoretical prediction, that the power dependence should be 2 for the metallic tubes, which are assumed to dominate the harmonic generation. This disagreement between experiment and the semiclassical theory can be due to the fact that the theory, while better suited for the metallic tubes, underestimates the contribution of the semiconducting tubes to the harmonic generation. This has been recently confirmed by an improved full quantum-mechanical study of the harmonic generation in CNTs [SMK02]. This study showed that the TH from semiconducting tubes should be slightly higher than the TH signal generated by metallic tubes. Moreover, the power dependence for the TH generated in semiconducting tubes by an input laser beam polarised parallel to the tubes is predicted in this quantum-theory to be 2.44, close to the value of 2.3 ± 0.1 measured here from samples of *not-aligned* tubes (for p-polarised input). The reason why the sample of aligned tubes with a slope of three behaves differently is not clear, since alignment effects were not taken into account yet, at this level of the theory.

Another aspect is that the theory predicts that no harmonics should be generated by a field perpendicular on the tube's axis. Fig.4.13 shows the dependence of the TH yield on the polarisation of the fundamental beam; the curves are normalised to the level of the TH signal generated by an s-polarised input. Surprisingly, an s-polarised laser beam generates a higher third harmonic output than a p-polarised beam, exactly the opposite of what theory predicts.

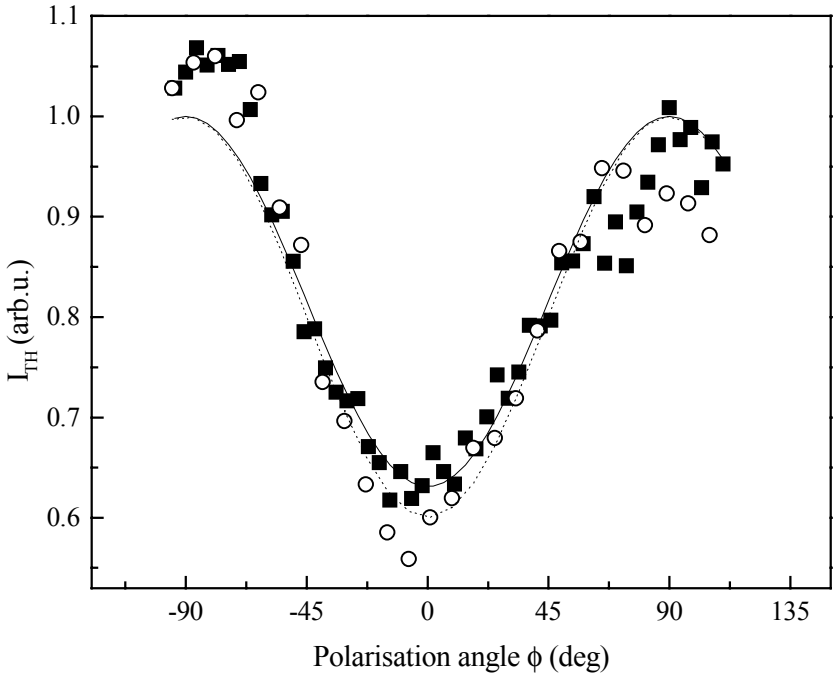

Fig.4.13. Normalised dependence of the TH intensity on the input polarisation. The polarisation angle is measured from the plane of incidents: 0° states for p-polarisation, 90° for s-polarisation. The TH output is unpolarised. Full squares and solid line: aligned MWCNTs; open circles and dotted line: not-aligned MWCNTs, both with diameters of 20 nm. The lines are data fits using a $\sin^2\phi$ function.

A possible explanation for this behaviour could be the oscillation of the electrons across their 2D cylindrical distribution, similar to the HHG generation mechanism in solids. In such a process, though, both odd and even harmonics are generated, which is not the case here. Fig.4.11 shows that only the third harmonic is enhanced from the broad continuum. Moreover, there is basically no difference in Fig.4.13 between the sample of aligned tubes and the sample containing tubes with random orientations. The apparent difference at the p-polarised input is not significant within the experimental errors (determined by long-time laser intensity variations and spot-to-spot differences on the samples). Different mechanisms for the harmonics generation from CNTs should therefore be considered, taking into account both axial and azimuthal electron surface currents.

The spectrum in Fig.4.11 shows no enhancement at the fifth harmonic wavelength of 250 nm. This wavelength range was investigated carefully for different samples with the same result. However, a significant signal can be detected at this wavelength. The laser power dependence for the generation at 250 nm, the fifth harmonic of the laser wavelength, was studied in detail for the sample of aligned MWCNTs and the two samples of not-aligned MWCNTs. Fig.4.14 shows that the intensities generated from the three samples do not differ significantly and no saturation

is observed, in contrast to the TH curves, which show saturation for driving fields higher than $4 \cdot 10^{10}$ W/cm^2.

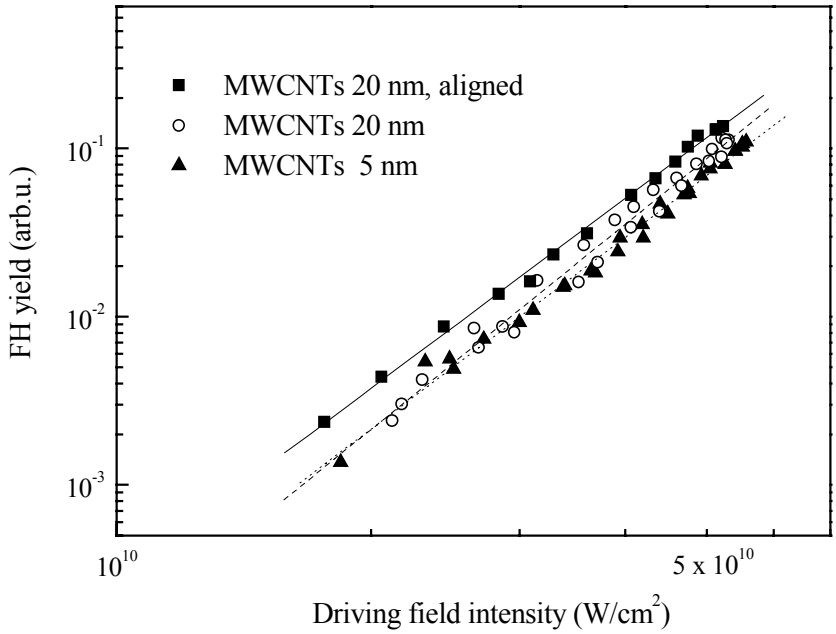

Fig.4.14. Power dependence of the FH at 250 nm, for a p-polarised fundamental.

At an input intensity of $1 \cdot 10^{11}$ W/cm^2 the theory (discussed in Chapter 4.2) is predicting an intensity of the TH by a factor of about 100 times higher than the intensity of the FH (see also Fig.4.5). In the logarithmic plot of the spectrum in Fig.4.11, the TH intensity level is more than two orders of magnitude higher than the noise level (corresponding to the points measured below 200 nm, where any signal is cut off). If fifth harmonic was generated in these films with the predicted efficiency (relative to the TH efficiency), it should be visibly enhanced from the continuum background. We thus conclude that the light at 250 nm is predominantly generated by the process responsible for the white light generation, and not through a harmonic generation mechanism.

Wavelength detected →	250 nm (FH)		220 nm	280 nm
input polarisation →	s	p	p	p
MWCNTs 20 nm, aligned	3.7	3.8	3.8	3.6
MWCNTs 20 nm	4.1	3.7	3.7	3.6
MWCNTs 5 nm	3.9	4.0	4.5	4.1

Table 4.2. Power dependence slopes for the FH at 250 nm for both s- and p-polarised driving field and for two wavelengths in the white continuum, at 220 and 280 nm, generated by a p-polarised incident beam; typical errors: ± 0.1.

4.3.5 Continuum generation

The interaction between high intensity laser pulses and carbon nanotubes is generating a broad, featureless continuum spectrum, as shown in Fig.4.11. This observation was made for all samples, regardless of the dimension of the tubes or their alignment. Fig.4.15 shows the continuum spectrum generated by the sample of aligned MWCNTs, when irradiated by an s-polarised fundamental with different intensities. The spectra, measured in steps of 5 nm, are corrected for the apparatus function; the structures appearing at higher wavelengths are due intensity fluctuations of the laser and are different from scan to scan. The insert shows two uncorrected spectra normalised in intensity, which are taken at $2.32 \cdot 10^{11}$ W/cm^2 (solid line) and at $1.34 \cdot 10^{11}$ W/cm^2 (dotted line). The uncorrected spectra illustrate the blue shift with increasing the intensity of the laser, which is less obvious after the correction. Such a broad continuum can be emitted either through a nonlinear process, namely self-phase modulation, by fluorescence, or by creating a local plasma.

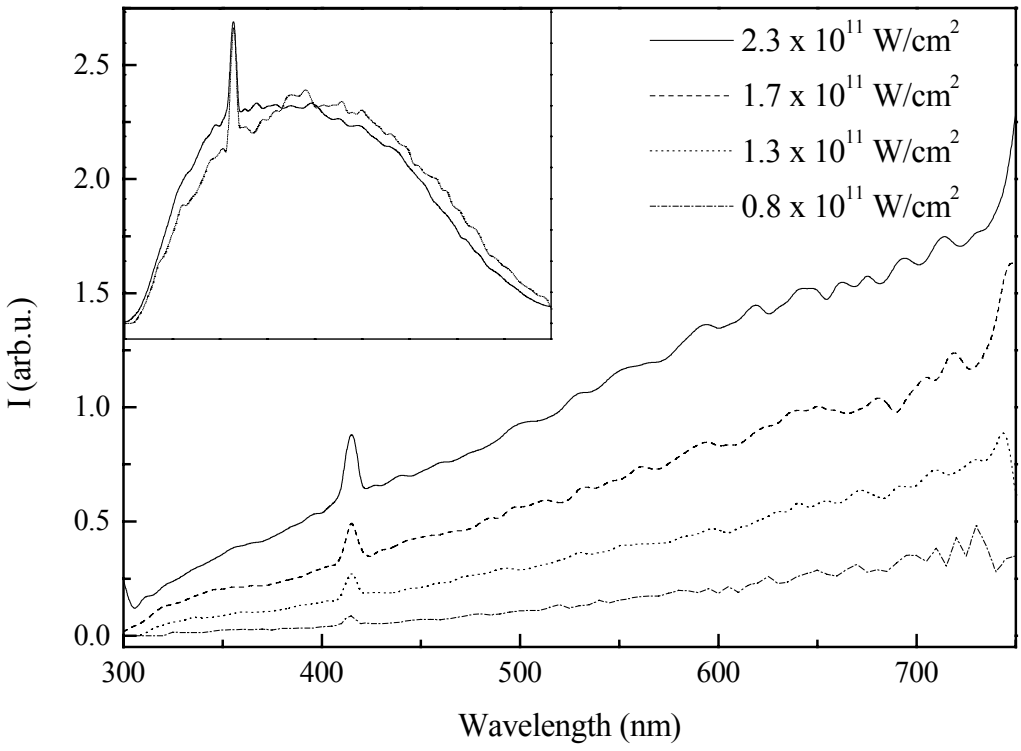

Fig.4.15. White light generated by the aligned MWCNTs, for different input intensities. The fundamental beam was s-polarised. The curves are corrected for the efficiencies of the monochromator, the photomultiplier and the transmission of the KG5 filters from the detection system. Insert: normalised, uncorrected spectra taken at $2.3 \cdot 10^{11}$ W/cm^2 (solid line) and at $1.3 \cdot 10^{11}$ W/cm^2 (dotted line).

An intense laser beam propagating through a medium changes the refractive index of this medium, which in turn changes the phase of the incident laser pulse – a process named self-phase modulation (SPM). The phase change can cause a frequency broadening within the pulse itself. In condensed media, broadening through SPM extends over ~ 2 - 300 nm around the wavelength of the incident laser beam. The intensity of the newly generated frequencies is normally within three orders of magnitude from the intensity of the input frequency (see, e.g. [SuC91, LGD96]). In materials with high-energy bandgap (> 5 eV), where self-focusing and multiphoton excitation contribute to the continuum generation, the broadening can extend over as much as 500 nm to shorter wavelengths [BrC98]. The wavelength of the driving beam used in these experiments, at 1250 nm, is far from the range of 300 - 750 nm that we studied. If the white light in our CNT samples were generated through self-phase modulation, this would mean that we measured the farthest tail of the very efficiently broadened input frequency.

The spectral broadening is in general reduced when generated with positively chirped input beams and enhanced for negative chirps [WHA89]. When measuring the white continuum, within our experimental range of 300-750 nm, generated with chirped pulses of 460 fs, no difference in the shape of the spectra generated with positively and negatively chirped pulses was found in our experiments. This is a first indication that SPM is not responsible for the generation of white light in our samples.

For a more clear confirmation of the broadening through SPM, one needs to measure the spectrum generated around the driving beam frequency. Our experimental window is mainly limited by the spectral range of the monochromator, between 200 and 800 nm. Therefore, we have also used the second harmonic of the Cr:forsterite laser at 625 nm as driving beam, to investigate whether SPM is indeed induced in the CNTs samples. Fig.4.16 shows the spectra measured for an s-polarised input beam of $1 \cdot 10^{11}$ W/cm^2 and $2.6 \cdot 10^{10}$ W/cm^2, both from the sample of aligned MWCNTs and, for a comparison, from a rough plate of BK7 glass. We used a rough, thus strongly scattering plate to have a comparable detection geometry for both samples. A filter BG1 was used in the path of the output scattered beam to block part of the fundamental; all spectra are corrected for the transmission of this filter. Despite this reduction of the fundamental, the photomultiplier was saturated between 600 and 650 nm. An increased background level of laser stray light compared to the 1250 nm experiments is detected (see Chapter 4.2 for details) over the whole spectral range. The spectrum reflected by the BK7 plate is broadened around the input wavelength of 625 nm when increasing the intensity of the incident beam, as expected for a self-phase modulation process. An overall increase of the signal

over the whole measured spectrum can also be observed. This increase is linear in the input intensity and comes most probably from the stray light inside the monchromator. In the case of the aligned MWCNTs, the peak at 625 nm is not broadened when increasing the input intensity. We can thus rule out the possibility that the white light generated by the samples of CNTs be generated through self phase modulation or a similar mechanism.

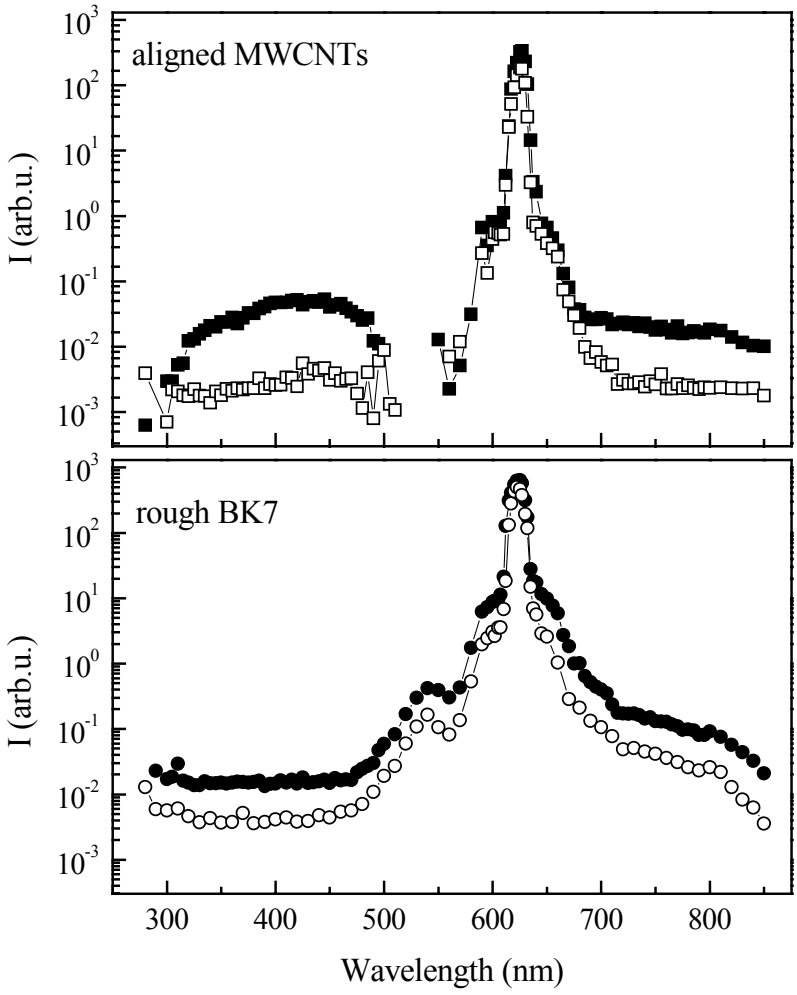

Fig.4.16. Reflected spectra of an s-polarised beam at 625 nm, with an intensity of $1 \cdot 10^{11}$ W/cm^2 (solid symbols) and $2.6 \cdot 10^{10}$ W/cm^2 (open symbols) from the sample of aligned MWCNTs and from a rough BK7 plate. The spectra are corrected for the transmission of the BG1 filter used in the output detection system.

In the low-intensity part, corresponding to the spectral ranges 300-550 nm and 700-850 nm, the increase in the signal is stronger for the CNTs than for the BK7 plate, and is also nonlinear in the input intensity, suggesting that another process than a scattered background contributes to the increase of this signal. The apparent minimum at ~ 580 nm is only due to the transmission window of the filter used in this measurement, and did not appear when different filters were used in the detection path.

Fluorescence due to multiphoton absorption in the CNTs can also explain the white light emission. The fact that the absorption spectra of the tubes, shown in Fig.4.8, do not show any pronounced resonant structures agrees well with the featureless continuum emitted under the high intensity laser irradiation. Luminescence of SWCNTs and MWCNTs was also observed during electron field emission [BSM98]. In these measurements, though, the emission extended only between 620 and 775 nm with a resonant peak at 700 nm, which is not observed in our measurements.

CNTs are also known as excellent field emitters [e.g. DWM99, CDR01], for electric fields higher than 10^6 V/m. The field strengths of our laser beams are of the order of 10^8 V/m. We propose that the high intensity laser pulse is generating free electrons from the samples of CNTs. The low-density plasma formed by the collision of these electrons with gas molecules in air (all these experiments were performed in air) could be responsible for the broad continuum, which was even observable by eye when irradiating the samples. A strong acoustic effect that can be heard when the laser hits the samples could also indicate the plasma expansion in air. The energy of the free electrons and the plasma density are increasing with increasing the laser intensity, so that the generated spectrum extends further into the blue, as observed in our experiments. It is important to note that the nanotubes were not destroyed and the emission was constant over the measuring time, extending up to one hour.

Different materials were investigated in order to see to what extend this continuum generation is specific to the carbon nanotubes. Fig.4.17a shows a measurement over the spectral range 300 - 750 nm, from aligned MWCNTs, SWCNTs, HOPG and rough BK7 glass irradiated with 1250 nm wavelength, at an intensity of $1.7 \cdot 10^{-11}$ W/cm^2. The spectra were acquired through a KG5 filter and are not corrected for the filter transmission. Fig.4.17b is an enlargement of these spectra around the third harmonic wavelength of 417, showing the low conversion efficiency of the MWCNTs compared to the other materials. The rough BK7 sample only shows a strong TH peak and a weaker second harmonic (SH) peak. Highly oriented pyrolytic graphite (HOPG) shows a fairly similar behaviour compared to the samples of nanotubes. The white light emission is, though, much weaker for this sample. Using electron energy loss spectroscopy and ultraviolet and X-ray photoemission spectroscopy, Chen et al. [CWS99] have reported that MWCNTs have a smaller work function and a stronger plasma excitation than graphite. The generation of free electrons is thus less efficient from HOPG than from MWCNTs, which can explain the weaker white light intensity generated from HOPG.

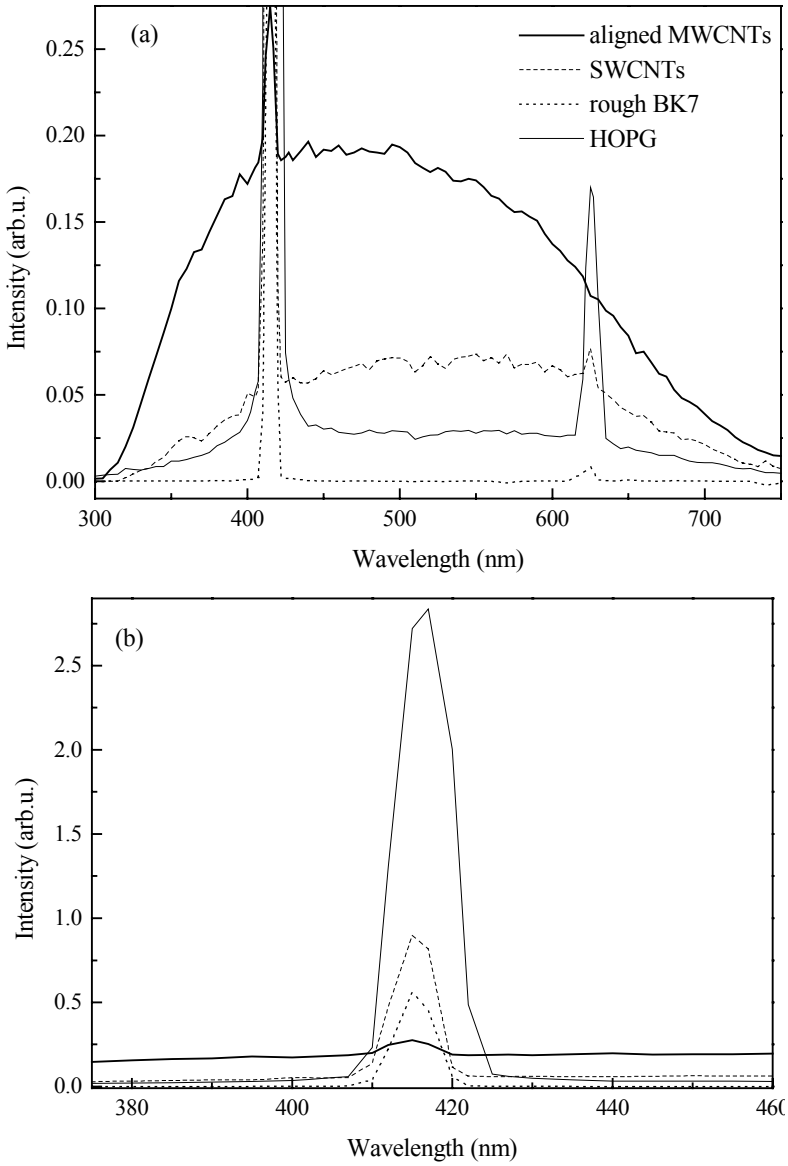

Fig.4.17. (a) White light induced by an s-polarised beam of $1.7 \cdot 10^{-11}$ W/cm^2 at 1250 nm, for different materials. The spectra are not corrected for the transmission of the KG5 filter. (b) Enlargement of (a) around the third harmonic wavelength, of 417 nm.

The sample of SWCNTs shows a broad continuum similar to the spectrum from the MWCNTs. The strong TH and the SH peaks could be due to the contribution of residual amorphous carbon impurities. The SWCNT spectrum is red-shifted, indicating that a lower-density plasma is generated in this case. The threshold of the driving field strength for the generation of free electrons is inversely proportional to the diameter of the tubes, according to equation (4.9). This means that the SWCNTs, having smaller diameters than the MWCNTs, should emit fewer electrons, therefore generating a less dense plasma with a red-shifted light emission, as found in these measurements.

4.4 Conclusions

The laser interaction with CNTs mainly results in the generation of a broad optical continuum, which is tentatively explained based on the fluorescence and the production of free electrons, exciting a non-destructive plasma in air. Only the third harmonic of the input laser frequency is enhanced from this broad continuum. The present work shows that the special predictions concerning the semiconducting tubes in the semiclassical theory are not supported by the experiments. This is in good agreement with the theoretical improvements to a full quantum-theoretical approach [SMK02]. The TH generation in the plasma should also be considered, provided that this plasma is formed in a time shorter than the laser pulse width of ~ 160 fs. More investigations are needed to clarify this process. The evident high efficiency of electron emission under the action of light recommends CNTs as pulsed electron emitters.

The damage threshold for films of CNTs deposited on silicon substrates and irradiated in air at 1250 nm is $5 \cdot 10^{11}$ W/cm^2. For a wavelength of 625 nm, the damage threshold is lower, namely $1.3 \cdot 10^{11}$ W/cm^2.

The sample of aligned MWCNTs used in these experiments is apparently not fully meeting the requirements imposed by the theory of harmonics generation described in [SMK99, SMK01]. The large diameters of the tubes favour the generation of free electrons, which dominates the response of the system to the laser excitation. Samples of aligned SWCNTs should be better candidates for future HHG measurements. They are closer to the theoretical requirements and there are better chances that the harmonics generation mechanism can dominate the electron emission in such samples. Aligned SWCNTs with diameters down to 0.7 nm [TSW98] and, more recently, 0.4 nm [LTL01] were grown by chemical vapour deposition (CVD) using metal-doped microporous $AlPO_4$ crystals. The disadvantage of these samples is that the tubes are embedded in the pores of an $AlPO_4$ crystal, so that the overall response of the system in an optical study would be an overlap between the response of the CNTs and that of the supporting medium. A chemical modification of the tubes can be expected when the supporting crystals are dissolved. More recently, perfectly ordered single crystals of identical SWCNTs were grown by thermolysis of nano-patterned C_{60}-Ni sandwiches [SSG01]. The dimensions of the crystals varied from tens of nanometres to micrometers, and these nanodomains were oriented with the tubes perpendicular to the substrate. The concentration of such crystals on the substrate is rather low, so that the substrate would have a high influence on optical measurements from such samples.